RSC Advances

PAPER

View Article Online
View Journal | View Issue

Cite this: *RSC Adv.*, 2022, **12**, 10142

DeNO$_x$ performance enhancement of Cu-based oxides *via* employing a TiO$_2$ phase to modify LDH precursors†

Yali Du,‡[a] Xuezhen Liu,‡[ab] Jiangning Liu,[b] Rongting Du[b] and Xu Wu *[bc]

Received 16th January 2022
Accepted 24th March 2022

DOI: 10.1039/d2ra00316c

rsc.li/rsc-advances

CuAl-LDO, CuAl-LDO/TiO$_2$ and CuAl-LDO/TiO$_2$NTs catalysts were obtained from TiO$_2$ modified LDHs precursor which were prepared by *in situ* assembly method. Then catalysts were evaluated in the selective catalytic reduction of NO$_x$ with NH$_3$(NH$_3$-SCR), and the results showed that the CuAl-LDO/TiO$_2$NTs catalyst exhibited preferable deNO$_x$ performance (more than 80% NO$_x$ conversion and higher than 90% N$_2$ selectivity at a temperature range of 210–330 °C) as well as good SO$_2$ resistance. With the aid of series of characterizations such as XRD, N$_2$ adsorption/desorption, XPS, NH$_3$-TPD, H$_2$-TPR, and *in situ* DRIFTS, it could be concluded that, doping TiO$_2$NTs afforded the catalyst larger specific surface area, more abundant surface chemisorption oxygen species and more excellent redox performance. Meanwhile, *In situ* DRIFTS evidenced that CuAl-LDO/TiO$_2$NTs catalyst has a strong adsorption capacity for the reaction gas, which is more conducive to the progress of the SCR reaction.

1 Introduction

Nitrogen oxides (NO$_x$), released from stationary sources (such as coal-fired power plants), are major atmospheric pollutants which seriously threaten the ecological environment and human health.[1,2] Selective catalytic reduction with NH$_3$ (NH$_3$-SCR) is considered as one of the most efficient technologies for removing NO$_x$.[3–5] Nowadays, the commercial V$_2$O$_5$-WO$_3$/TiO$_2$ catalysts are widely applied in the NH$_3$-SCR field and exhibit excellent catalytic activity in the temperature range of 300–400 °C.[3,6,7] However, there are still some practical problems of the catalysts, such as the toxicity of vanadium, low N$_2$ selectivity due to the formation of N$_2$O and high conversion of SO$_2$ to SO$_3$ at high temperature.[8,9] Generally, the poison of SO$_2$ and dust can be avoided by placing an SCR reactor behind the dust removal and desulfurization equipment, resulting in the debasement of exit gas temperature, which cannot meet the optimum activity temperature window of V$_2$O$_5$-WO$_3$/TiO$_2$ catalysts.[10–12] Thus, it would be necessary to develop more efficient and eco-friendlier deNO$_x$ catalysts with non-vanadium-based at low temperatures.

At the present stage, many researchers consider the copper oxides as a potential candidate for the low-temperature SCR catalysts, including pure copper oxides, copper-based composite oxides and supported copper-based catalysts.[13–16] Among them, copper-based composite oxides catalysts with excellent catalytic performance have recently attracted much attention. In recent years, it is well known that layered double oxides (LDO) from layered-double hydroxides (LDHs) demonstrated fine reaction activity in NH$_3$-SCR, especially the typical CuAl-LDO catalyst.[17,18] For instance, Yan *et al.* reported a high-performance Cu-based oxides catalyst prepared from CuAl-LDHs precursor.[19] In our previous work, it is also found that the CuAl-LDO catalysts derived from LDHs demonstrated better reaction activity in NH$_3$-SCR.[18] However, due to its insufficient acidity, the CuAl-LDO catalyst afforded poor reaction activity at medium and high temperature in NH$_3$-SCR, which limited its further application.

As well known, titanium dioxide (TiO$_2$) has been found to be a valuable and environmentally friendly material with stable chemical properties.[20] At the same time, for transition metal oxide catalyst, the introduction of TiO$_2$ could improve the acid sites and chemical adsorption oxygen over the catalyst surface, enhance the adsorption and activation of NH$_3$ as well as resistance of SO$_2$.[21–24] Based on the characteristic advantages of LDHs and TiO$_2$, it is promising to prepare well-behaved Cu–Ti composite oxide catalysts derived by LDHs. However, due to the Jahn–Teller distortion of Cu^{2+} ions, it is difficult to prepare CuTi-based LDHs by one step preparation. Here, desirable SCR catalyst of CuAl-LDO/TiO$_2$ was tentatively fabricated by modifying CuAl-LDHs with TiO$_2$ phase.

[a]*College of Chemistry and Chemical Engineering, Jinzhong University, Jinzhong 030619, P. R. China*

[b]*College of Chemistry and Chemical Engineering, Taiyuan University of Technology, Taiyuan 030024, P. R. China. E-mail: wuxu@tyut.edu.cn; Fax: +86-351-6018528; Tel: +86-351-6018528*

[c]*Shanxi Huadun Industrial Co., Ltd, Taiyuan 030062, China*

† Electronic supplementary information (ESI) available. See DOI: 10.1039/d2ra00316c

‡ These authors contributed equally to this work.

Herein, the CuAl-LDHs with titanium-based materials were assembled and calcined at high temperature. Subsequently, the catalytic performance of the obtained composite oxide catalysts was evaluated in NH_3-SCR reaction. At the same time, the structural characteristics and the SCR performance of the catalysts were explored through a series of characterizations, such as XRD, N_2 adsorption/desorption, TEM, XPS, H_2-TPR, NH_3-TPD. The intrinsic difference between CuAl-LDO and CuAl-LDO/TiO_2-NTs catalysts derived by LDHs over the deNO_x activity was studied by *In situ* DRIFTS. This research might provide significant reference value for LDHs precursor in SCR application.

2 Materials and methods

2.1. Materials

TiO_2(P25), $Cu(NO_3)_2\cdot 3H_2O$(99%), $Al(NO_3)_3\cdot 9H_2O$(99%), NaOH(96%) and Na_2CO_3(99%) were obtained from the Sinopharm Chemical Reagent Company. All chemicals were of analytical grade and were employed without further purification.

2.2. Sample preparation

2.2.1. Synthesis of TiO_2NTs. The titanium-based materials used in this study were TiO_2(P25) and TiO_2 nanotubes (TiO_2-NTs) where the TiO_2NTs were synthesized by hydrothermal method *via* TiO_2(P25) as the precursor. The specific procedure is as follows: the P25 was added to the NaOH solution (10 M) to form a homogeneous mixture. After that, the mixture was transferred into a Teflon autoclave and reacted at 150 °C for 30 h. The slurry was filtered and washed initially with deionized water until the pH reached about 7 and mixed with 0.1 M H^+ solution to reach a pH value about 1. Finally, the obtained precipitate was washed until the filtrate was neutral and dried at 70 °C for 30 h. Then, the obtained powder was calcined at 400 °C for 2 h (the heating rate being 2 °C min^{-1}) to obtain titanium dioxide nanotubes (marked as TiO_2NTs).

2.2.2. Preparation of catalyst. The CuAl-LDHs/TiO_2NTs and CuAl-LDHs/TiO_2 precursors were prepared by *in situ* assembly method. In detail, a certain amount of TiO_2NTs or TiO_2 was dispersed in 100 mL deionized water to form dispersion liquid (solution A). The mixed nitrate solution (0.12 M $Cu(NO_3)_2\cdot 3H_2O$ and 0.04 M $Al(NO_3)_3\cdot 9H_2O$) and mixed base solution (0.3 M NaOH and 0.1 M Na_2CO_3) were slowly dripped into a round-bottomed flask within solution A. After that, the mixed solution was hydrothermally treated at 65 °C for 10 h. The obtained LDHs slurry was filtered and washed, dried overnight at 70 °C to obtain LDHs powder which was denoted as CuAl-LDHs/TiO_2NTs or CuAl-LDHs/TiO_2. The CuAl-LDHs were also fabricated *via* the identical method without any addition of titanium dioxide in solution A. Then CuAl-LDO, CuAl-LDO/TiO_2NTs and CuAl-LDO/TiO_2 catalysts were prepared *via* calcining LDHs powders at 500 °C for 5 h under nitrogen (80 mL min^{-1}).

2.3. Catalyst characterization

The phase structure of the LDHs and catalyst samples was analyzed by the Rigaku DX-2700 X-ray diffractometer instrument, with Cu/Kα radiation ($\lambda = 1.54184$ Å) at the 2θ of 5° to 85°. The morphology of the precursors was scanned and analyzed by the scanning electron microscope (SEM, Hitachi's SU8010 JEOL). The morphology and surface atomic concentration of catalyst was scanned and analyzed by SEM and EDS-mapping (Carl Zeiss GeminiSEM300, Germany). The surface textural structures of catalysts were operated on the ASAP-2460 physical adsorption instrument (Micromeritics, USA) at −196 °C. Brunauer–Emmett–Teller (BET) method and Barrett–Joyner–Halenda (BJH) model were used to calculated the specific surface area, pore volume and pore diameter of catalysts. The transmission electron microscope (TEM) analysis was used to research the morphology images of the catalysts by JEM-2100F, JEOL microscope with an accelerating voltage of 200 kV. The surface property of the catalysts was analyzed by X-ray photoelectron spectroscopy (XPS, Thermo Fisher ESCALAB 250xi, England) with Al Kα radiation ($h\nu$ = 1486.6 eV). Both NH_3-temperature programmed desorption (NH_3-TPD) and H_2 temperature-programmed reduction (H_2-TPR) tests were performed on the FINESORB-3010 temperature programmed adsorption instrument (Zhejiang Pantech) with using 80 mg catalysts. For NH_3-TPD test, the catalysts were pretreated in He atmosphere at 150 °C for 1 h, and then cooled to 50 °C in the same stream. Then the input gas was shifted a 3% NH_3 + He (25 mL min^{-1}) mixed atmosphere at 50 °C, and the adsorption in this atmosphere lasted for 30 minutes. Before starting the TPD experiment, the catalyst was flushed with He at a flow rate of 30 mL min^{-1} to remove physically adsorbed NH_3 on its surface. The desorption process was performed by heating the samples in He (30 mL min^{-1}) from 50 °C to 600 °C at a heating rate of 10 °C min^{-1}, the data was detected and recorded online by a thermal conductivity detector (TCD), then analyzed by the Origin software. Each desorption peak was integrated to obtain the corresponding peak area, as well as the total acid content and the ratio of strong and weak acid sites were calculated. For H_2-TPR experiment, 80 mg catalyst (particle size: 40–60 mesh) was putted into a laboratory-made quartz tube, and pre-treated in pure Ar atmosphere (flow rate: 20 mL min^{-1}) for 1 h at 300 °C. Then cooled down the temperature to 30 °C and stabilize for a period of time, followed by changing the gas to 10% H_2/Ar, and the reduction process occurred from 30 °C to 600 °C at a heating rate of 10 °C min^{-1}. The corresponding data was detected and recorded by TCD. Origin software was employed to fit the H_2-TPR curve through splitting the peaks, and calculate the hydrogen consumption based on the peak area. *In situ* diffuse reflectance infrared Fourier transform spectroscopy (*In situ* DRIFTS) experiments were performed using *In situ* infrared spectrometer (Bruker TENSOR 27) from Germany, with a Pike DRIFTS sample cell and a high-precision MCT detector cooled by liquid nitrogen. At first, the sample was pretreated at 300 °C under N_2 about 10 min, and the background spectrum was collected in the same condition at the test temperature (240 °C). Then, each spectrum was recorded by subtracting the background spectrum in the range of 2000–1000 cm^{-1}. The gas flow during reaction process included: 600 ppm NO, 600 ppm NH_3, 5 vol% O_2, 100 ppm SO_2, with N_2 as the balance gas. The acid sites over the samples were investigated by infrared spectroscopy of adsorbed pyridine (Py-IR) using Bruker INVENIO S from Germany. The spectra were recorded with

2 cm^{-1} spectral resolution on a Frontier FT-IR Spectrometer at 240 °C.

2.4. SCR activity test

The NH_3-SCR performance of the catalysts (40–60 mesh) was tested over the fixed-bed quartz tube reactor. The reaction gas was set as follows: 600 ppm NO, 600 ppm NH_3, 5 vol% O_2, 100 ppm SO_2 (when used), with N_2 as the balance gas and the space velocity (GHSV) was 45 000 h^{-1}. Experimental configurations for evaluating catalytic performance were presented in Fig. S1.†

The IR flue gas analyser (MKS) was hired to detect online gas concentration and recorded the reaction data in a steady state at each temperature point (from 150–360 °C with 30 °C as an interval). NO_x conversion and N_2 selectivity were calculated by eqn (1) and (2):

$$NO_x \text{ conversion } (\%) = \frac{[NO_x]_{in} - [NO_x]_{out}}{[NO_x]_{in}} \times 100\% \quad (1)$$

$$N_2 \text{ selectivity } (\%) = \frac{[NO_x]_{in} + [NH_3]_{in} - [NO_x]_{out} - [NH_3]_{out} - 2[N_2O]_{out}}{[NO_x]_{in} + [NH_3]_{in} - [NO_x]_{out} - [NH_3]_{out}} \times 100\% \quad (2)$$

In the above formula, the subscript "$[X]_{in}$" and "$[X]_{out}$" indicate the inlet and outlet concentration of gas in a steady state flow mode, respectively.

3 Results and discussion

3.1. Catalytic performance of the catalysts

3.1.1. Catalytic activity and N_2 selectivity. The deNO_x performance of CuAl composite oxide catalysts (CuAl-LDO, CuAl-LDO/TiO_2 and CuAl–TiO_2NTs) were tested from 150 °C to 360 °C, and the results are shown in Fig. 1. It can be seen from Fig. 1 that modifying CuAl-LDO catalyst by different Ti-based materials significantly improved the NH_3-SCR performance. As displayed in Fig. 1(A), the catalytic activity of CuAl-LDO catalyst was better than the CuAl-LDO/TiO_2 and CuAl-LDO/TiO_2NTs catalysts below 240 °C, the catalytic activity of CuAl-LDO/TiO_2 catalyst was better than that of the CuAl-LDO and CuAl-LDO/TiO_2NTs catalysts above 300 °C. However, at the test temperature ranges of 210–330 °C, the CuAl-LDO/TiO_2NTs catalyst showed better catalytic activity with above 80% NO_x conversion than other catalysts. As demonstrated in Fig. 1(B), the N_2 selectivity of all catalysts showed clear downward trend with increasing temperature, suggesting that the N_2 selectivity was susceptible to ammonia oxidation at high temperature. During the whole test temperature range, CuAl-LDO catalyst afforded lowest selectivity while the CuAl-LDO/TiO_2NTs presented best N_2 selectivity of more than 90% in 150–360 °C, as well as higher than 80% for CuAl-LDO/TiO_2. The results indicated that the NH_3-SCR performance of CuAl-LDO catalyst was observably affected by introducing different Ti-based materials. In addition, the stability of CuAl-LDO/TiO_2NTs catalyst was tested and results are shown in Fig. S2.† As presented, the better catalytic activity of CuAl-LDO/TiO_2NTs catalyst was kept even after seven cycle tests, indicating the superior stability.

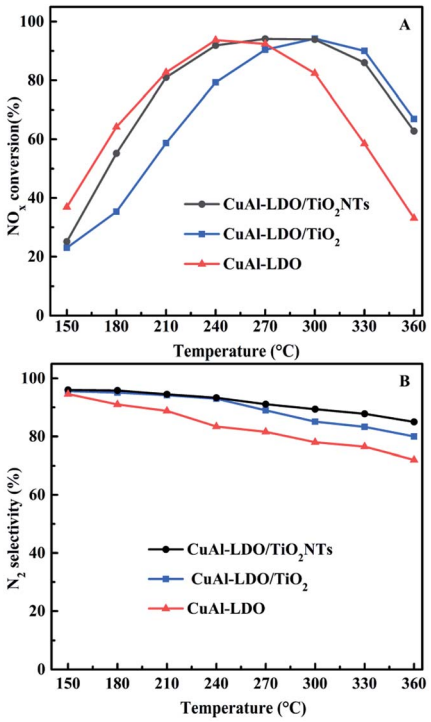

Fig. 1 The (A) NO_x conversion, (B) N_2 selectivity of catalysts.

3.1.2. The SO_2 resistance test. In NH_3-SCR reaction, the catalyst is usually deactivated by the SO_2 in the flue gas. So, the catalysts with excellent SO_2 durability are vital in practical process. Therefore, the SO_2 resistance of CuAl-LDO and CuAl-LDO/TiO_2NTs catalysts at 240 °C were tested and the corresponding results are displayed in Fig. 2. As shown in Fig. 2, after adding SO_2 into flue gas, the NO_x conversion decreased from 92% to 80% for CuAl-LDO/TiO_2NTs catalyst and 93% to 70% for

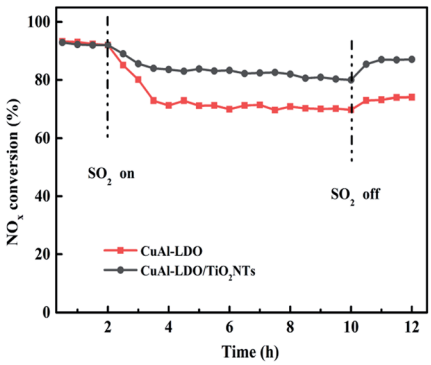

Fig. 2 SO_2 resistance test over CuAl-LDO/TiO_2NTs and CuAl-LDO catalysts at 240 °C. Reaction conditions: [NO] = [NH_3] = 600 ppm, [O_2] = 5 vol%, [SO_2] = 100 ppm, N_2 as balance gas, under a GHSV of 45 000 h^{-1}.

CuAl-LDO catalyst, respectively. After the SO_2 were purged off, the activity recovered to 86% for the CuAl-LDO/TiO_2NTs catalyst, but only 73% for CuAl-LDO catalyst. The results indicated that the CuAl-LDO/TiO_2NTs catalysts possessed better SO_2 resistance than CuAl-LDO catalyst. The capacity of SO_2 adsorption over both catalysts were researched by *In situ* DRIFTS measurement as shown in the Fig. S3.† The results displayed that the intensity of SO_2 adsorption peaks and the species of sulfate over CuAl-LDO were higher than CuAl-LDO/TiO_2NTs. As summary, it is difficult to form sulfate on the surface of CuAl-LDO/TiO_2NTs catalyst after the introduction of SO_2, which was consistent with the result of resistance SO_2 performance test.

3.2. XRD patterns and SEM images of LDHs precursors

The XRD patterns of TiO_2, TiO_2NTs (prepared by the hydrothermal method), CuAl-LDHs, CuAl-LDHs/TiO_2 and CuAl-LDHs/TiO_2NTs are presented in Fig. 3. For TiO_2 and TiO_2NTs, it could be confirmed that the diffraction peaks at 25.3°, 37.8°, 48.1°, 53.9°, 55.1°, 62.7°, 68.8°, 70.3° and 75.1° might be assigned to the crystal planes of anatase TiO_2 phase (JCPDS # 21-1272).[20,23] The peaks located at 11.9°, 23.8°, 34.8°, 39.1° and 60.9° in CuAl-LDHs, CuAl-LDHs/TiO_2 and CuAl-LDHs/TiO_2NTs were corresponded to the (003), (006), (012), (015) and (110) crystal planes of LDHs (JCPDS # 35-0964), respectively, indicating the successful preparation of LDHs precursors.[18,19] For CuAl-LDHs/TiO_2NTs and CuAl-LDHs/TiO_2, the peaks around 25.28°, 36.95°, 37.80° and 48.05° could be ascribed to the (101), (103), (004) and (200) of anatase. The TEM images of TiO_2NTs are presented in Fig. S4(A) and (B).† The TiO_2NTs has a regular morphology and a complete hollow tubular structure.

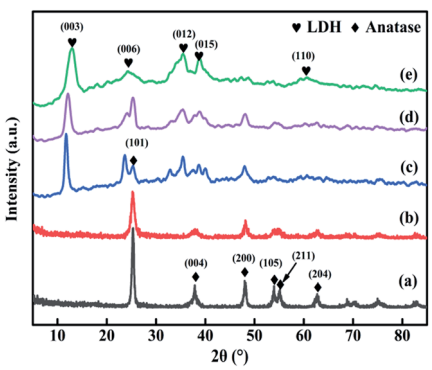

Fig. 3 The XRD patterns of (a) TiO_2(P25), (b) TiO_2NTs, (c) CuAl-LDHs/TiO_2NTs, (d) CuAl-LDHs/TiO_2 and (e) CuAl-LDHs.

The SEM images of CuAl-LDHs, CuAl-LDHs/TiO_2 and CuAl-LDHs/TiO_2NTs are displayed in Fig. 4. It could be seen from SEM images that all samples displayed morphology of assembled nanosheets, which was the typical structure of LDHs, thus further witnessing the successful preparation of LDHs. As shown Fig. 4(C), the nanosheets of CuAl-LDHs/TiO_2NTs were effectively separated by TiO_2NTs, which effectively alleviates the stacking and aggregation of LDHs laminates.

3.3. Characterization of the catalysts

3.3.1. XRD analysis. The XRD spectra of CuAl-LDO, CuAl-LDO/TiO_2 and CuAl-LDO/TiO_2NTs catalysts are shown in Fig. 5. As can be seen in Fig. 5, all catalysts presented the diffraction peaks of CuO (JCPDS #02-1040), while for the CuAl-LDO/TiO_2-NTs catalyst, the peaks at 36.4° and 42.3° corresponding to Cu_2O crystalline phase (JCPDS # 05-0667). In addition, the diffraction peak located at 25.35° for CuAl-LDO/TiO_2 and CuAl-LDO/TiO_2NTs catalysts can be attributed to TiO_2 (JCPDS # 21-1272).

3.3.2. N_2 adsorption/desorption analysis. The N_2 adsorption–desorption isotherms and pore diameter distribution curves of CuAl-LDO, CuAl-LDO/TiO_2 and CuAl-LDO/TiO_2NTs catalysts are showed in Fig. S5.† According to Fig. S5(A),† all samples displayed isotherms of type III which exhibited hysteresis loops mostly of type H3, indicating mesoporous structure of catalysts. The pore diameter distribution curves of catalysts were calculated by the Barrett–Joyner–Halenda (BJH) model as shown in Fig. S5(B).† It can be found that the CuAl-LDO/TiO_2NTs catalyst had more abundant pore structures than others. The BET specific surface area, pore volume and pore size of different catalysts are listed in Table 1. As shown in Table 1, the specific surface area, pore volume and pore diameter of CuAl-LDO/TiO_2 and CuAl-LDO/TiO_2NTs catalysts increased in comparison to that of CuAl-LDO catalysts. Meanwhile, the specific surface area sequence of the three catalysts was CuAl-LDO/TiO_2NTs (80.5 m^2 g^{-1}) > CuAl-LDO/TiO_2 (51.7 m^2 g^{-1}) > CuAl-LDO (49.7 m^2 g^{-1}), hinting that the surface area of CuAl-LDO/TiO_2NTs catalyst increased more significantly. The abundant pore structures and larger surface area of CuAl-LDO/

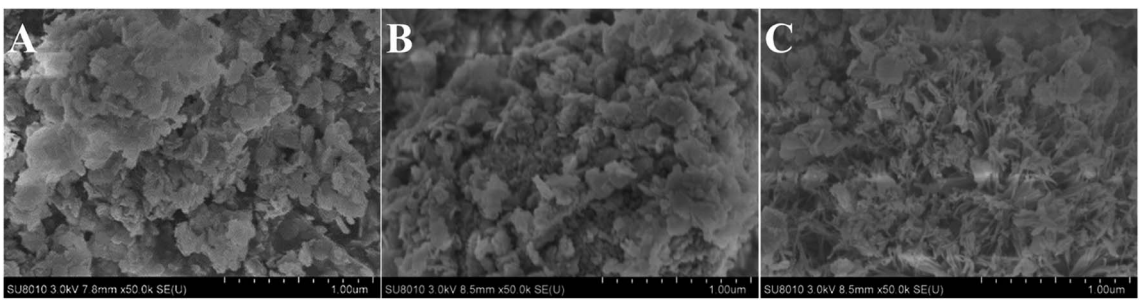

Fig. 4 The SEM images of the precursors: (A) CuAl-LDHs, (B) CuAl-LDHs/TiO_2 and (C) CuAl-LDHs/TiO_2NTs.

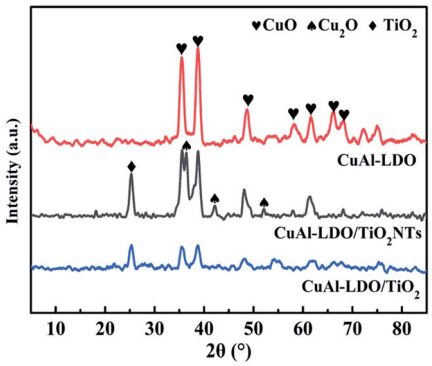

Fig. 5 The XRD patterns of catalysts.

Table 1 The specific surface area, pore volume and pore size of catalysts

Catalysts	S_{BET} (m^2 g^{-1})	Pore volume (cm^3 g^{-1})	Pore diameter (nm)
CuAl-LDO	49.7	0.35	27.3
CuAl-LDO/TiO_2	51.7	0.48	34.6
CuAl-LDO/TiO_2NTs	80.5	0.67	28.7
TiO_2	55.8	0.19	14.8
TiO_2NTs	192.8	0.8	15.2

TiO_2NTs catalyst was not only conducive to the explosion of active centers but also beneficial to the adsorption and activation reaction gases, thus leading to the better SCR activity, being consistent with the previous literature.[25]

3.3.3. TEM analysis. The microstructure of all catalysts was investigated by TEM tests and the results are shown in Fig. 6. It can be seen form Fig. 6(A)–(C), the thin layers still existed in CuAl-LDO, CuAl-LDO/TiO_2 and CuAl-LDO/TiO_2NTs catalyst during the annealing process. For CuAl-LDO/TiO_2NTs catalyst, it could be observed that the hollow tubular structure of TiO_2-NTs was maintained after roasting. During the LDHs annealing process, it could effectively slow down the stacking phenomenon of LDHs laminates, thereby facilitating the adsorption of reaction gas and accelerating the SCR reaction. Besides, the HR-TEM image (Fig. 6(D)) of the CuAl-LDO/TiO_2NTs presented two different lattice fringes, corresponding to the (111) crystal plane of CuO and (101) crystal plane of anatase (TiO_2), respectively. This conclusion was consistent with the results of XRD.

3.3.4. SEM & EDS-mapping analysis. The morphology and surface atomic concentration of the CuAl-LDO/TiO_2NTs catalyst were investigated by SEM and EDS-mapping analysis and the results are presented in Fig. 7. It was observed in Fig. 7(A) that the CuAl-LDO/TiO_2NTs catalyst could maintain the "flower-like" morphology after calcination. In Fig. 7(B)–(F), the EDS-mapping was applied to carry out the surface atomic concentration analysis of CuAl-LDO/TiO_2NTs catalyst. It was presented that the molar ratio of Cu/Al was about 2.8. The EDS mapping images of Cu, O, Al and Ti elements are shown in Fig. 7(C) and (D). The overlapping of all elements of Cu, O, Al and Ti verified a uniform distribution of all elements of CuAl-LDO/TiO_2NTs catalyst.

3.3.5. XPS analysis. The XPS tests were employed to study the surface element composition and electronic interaction of catalysts. The Cu $2p_{3/2}$, Cu LMM XAES and O1s spectra are presented in Fig. 8, coupled with the relative calculated parameters from the fitting curves as listed in Table 2. In Fig. 8(A), the Cu $2p_{3/2}$ spectra at 930–937 eV of all catalysts could be divided into two peaks, corresponding to Cu^{2+} (~934 eV) and Cu^+ (~932 eV) or Cu^0 (~932 eV), respectively.[19] The peaks at 940–945 eV of all these catalysts were attributed to the satellite peak of Cu^{2+}. Usually, the binding energy of Cu^0 was similar to that of Cu^+, thus the Cu LMM XAES spectrums were tested to distinguish them as displayed in Fig. 8(B).[26] It can be seen from Fig. 8(B) that all catalysts presented the peaks located at 912–914 eV and 917 eV, which could be assigned to Cu^+ (912–914 eV) and Cu^{2+} (917 eV). In addition, the CuAl-LDO/TiO_2NTs catalyst showed the peak at ~921 eV, contributing to the characteristics of Cu^0.[18] Meanwhile, the relative intensity of $Cu^+/(Cu^{2+} + Cu^+)$ was calculated as demonstrated in Table 2, with the following order: CuAl-LDO (38.4%) > CuAl-LDO/TiO_2NTs (33.4%) > CuAl-LDO/TiO_2 (24.1%). Therefore, the synergistic effect between Cu^+ and Cu^{2+} seems to be the main reason for the good deNO_x performance at low temperature range.

The O 1s spectra of the CuAl-LDO, CuAl-LDO/TiO_2 and CuAl-LDO/TiO_2NTs catalysts are showed in Fig. 8(C). As displayed in Fig. 8(C), the peaks at 530 eV could be assigned to the lattice oxygen species (denoted as O_I), accompanied by the chemisorbed oxygen species (denoted as O_{II}) located at 532 eV, which was closely related with the number of surface oxygen vacancies and defects of catalyst. Moreover, the peak at 533 eV for CuAl-LDO catalyst was corresponded to the adsorbed molecular water (denoted as O_{III}).[27,28] Besides, due to the high mobility ratio, O_{II} species were beneficial to the NO → NO_2 process and favored to the "fast SCR" reaction, thus resulting in the enhancement of low temperature SCR activity.[8] As listed in Table 2, the relative concentrations of $O_{II}/(O_I + O_{II})$ for CuAl-LDO/TiO_2NTs (65.2%) was higher than CuAl-LDO (54.4%) and CuAl-LDO/TiO_2 (62.3%). It could be concluded that the CuAl-LDO/TiO_2NTs owned more abundant surface oxygen than CuAl-LDO and CuAl-LDO/TiO_2, which might be helpful to the improvement of catalytic activity.

3.3.6. H_2-TPR analysis. The redox ability of catalysts is closely related to the NH_3-SCR performance, thus the H_2-TPR technique has been widely used and the results are showed in Fig. 9. Meanwhile, the reduction peak temperature and H_2 consumption of each catalyst are listed in Table 3. Two reduction peaks could be observed over TPR profiles for all catalysts. The first peak at 190 °C (CuAl-LDO), 224 °C (CuAl-LDO/TiO_2NTs) and 285 °C (CuAl-LDO/TiO_2) might be assigned to the reduction of highly dispersed CuO particles, being related to the reduction of Cu^{2+} → Cu^+ → Cu.[29,30] While the second peak located at 240 °C (CuAl-LDO), 271 °C (CuAl-LDO/TiO_2NTs) and 327 °C (CuAl-LDO/TiO_2) could be attributed to the reduction of the small crystalline CuO, the results above are consistent with the XRD results in Fig. 5.[30] As presented in Fig. 9(A), both peaks for CuAl-LDO/TiO_2NTs catalyst shifted to lower temperature comparing with CuAl-LDO/TiO_2, indicating the better reduction

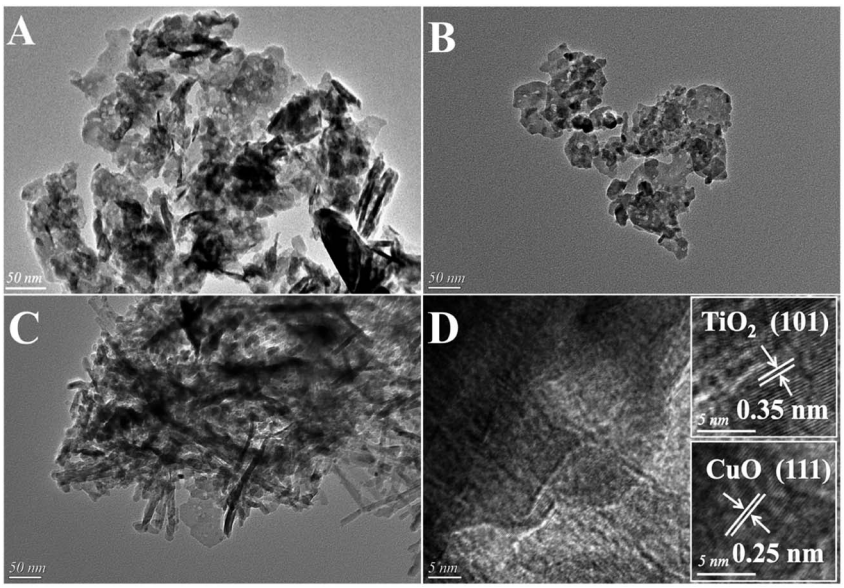

Fig. 6 The (A–C) TEM and (D) HR-TEM images of catalysts: (A) CuAl-LDO, (B) CuAl-LDO/TiO_2 and (C and D) CuAl-LDO/TiO_2NTs.

ability of the former one, which might be profited from the property of TiO_2NTs further resulting in the higher NO_x conversion of CuAl-LDO/TiO_2NTs catalyst at low temperature. It was noteworthy that the reduction temperature of CuAl-LDO/TiO_2NTs catalyst was slightly higher than CuAl-LDO, which was consistent with the results of low temperature NH_3-SCR activity.

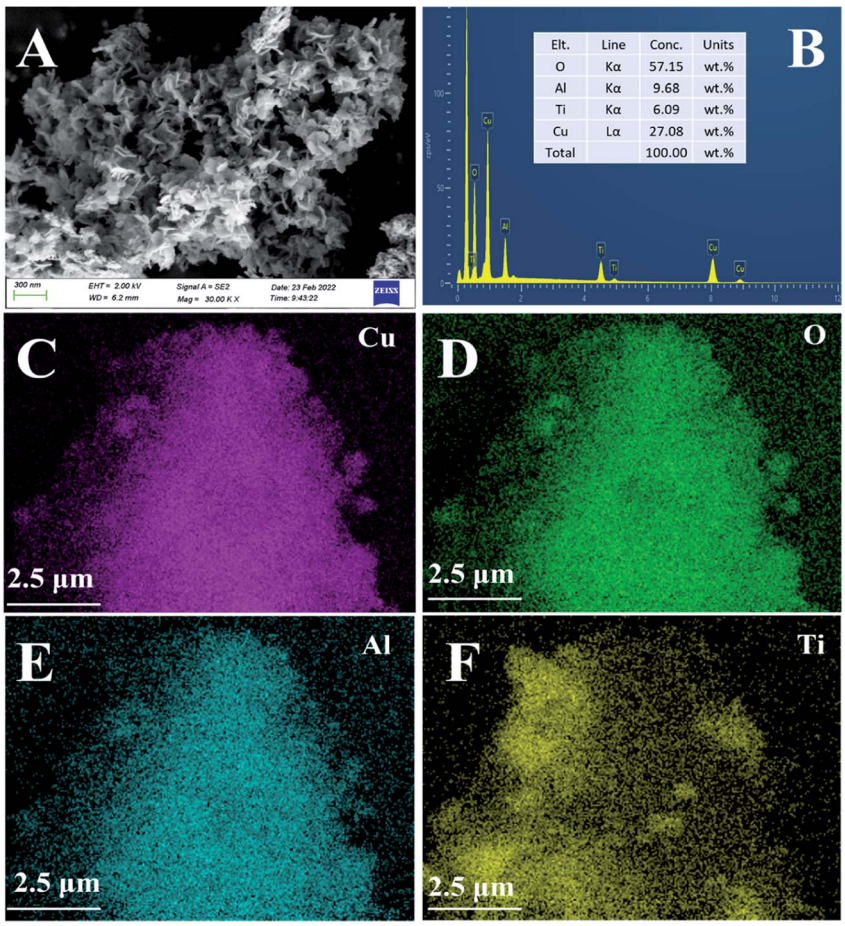

Fig. 7 The (A) SEM images and (B–F) EDS-mapping of CuAl-LDO/TiO_2NTs catalyst: (C) Cu, (D) O, (E) Al and (F) Ti.

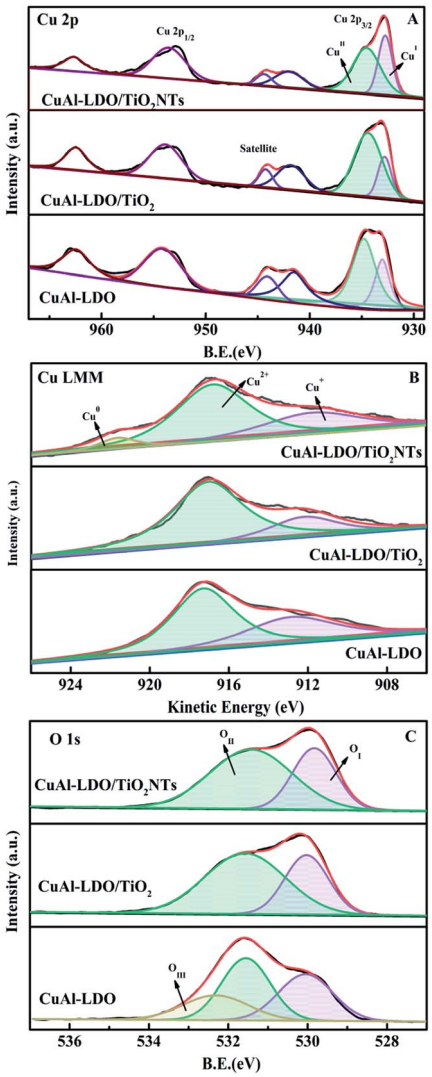

Fig. 8 The XPS spectra of the CuAl-LDO, CuAl-LDO/TiO_2 and CuAl-LDO/TiO_2NTs catalysts: (A) Cu 2p, (B) Cu LMM XAES, and (C) O 1s.

Table 2 The surface components of catalysts obtained by XPS analysis

	Cu LMM XAES kinetic energy (eV)			Relative concentration ratio/%	
Catalysts	Cu^+	Cu^{2+}	Cu^0	$Cu^+/(Cu^{2+} + Cu^+)$[a]	$O_{II}/(O_I + O_{II})$
CuAl-LDO	913.0	917.4	—	38.4	54.4
CuAl-LDO/TiO_2	914.0	917.2	920.6	24.1	62.3
CuAl-LDO/TiO_2NTs	913.1	917.0	921.4	33.7	65.2

[a] Intensity ratio between Cu^+ and (Cu^+ + Cu^{2+}) by deconvolution of Cu LMM XAES spectra.

Moreover, the calculated results shown in Table 3 further illuminating that the CuAl-LDO/TiO_2NTs catalyst with higher H_2 consumption was more favorable for the redox reaction.

3.3.7. NH_3-TPD analysis. In addition to redox ability, the acidity of catalyst was also the main factor for SCR activity. The NH_3-TPD profiles of CuAl-LDO, CuAl-LDO/TiO_2 and CuAl-LDO/TiO_2NTs catalysts are shown in Fig. 10, which researched the quantity and intensity of acidity over the catalyst surface. The relative acid contents of the catalysts calculated by normalizing the area of the NH_3 desorption peak of CuAl-LDO catalyst are listed in Table 3. It can be seen from the Fig. 10 that the CuAl-LDO catalyst showed a larger NH_3 desorption peak at 140 °C, indicating the existence of more weak acid sites. Compared with CuAl-LDO catalyst, the CuAl-LDO/TiO_2 and CuAl-LDO/TiO_2NTs catalysts presented significantly desorption peaks near 300 °C and 270 °C, respectively, which contributed to the medium-strong acid sites. While the small desorption peak located at around 530 °C for three catalysts could be assigned to the ammonia desorption from strong acid sites. As summarized in Table 3, the total amount of acid sites over CuAl-LDO/TiO_2NTs catalyst was richer than CuAl-LDO and CuAl-LDO/TiO_2 catalysts, which could be attributed to the outstanding catalytic performance of the CuAl-LDO/TiO_2NTs catalyst in the total test temperature range.[31]

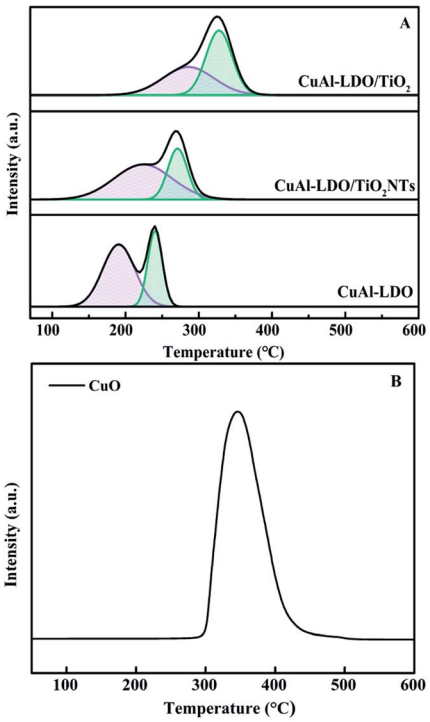

Fig. 9 The H_2-TPR profiles of (A) catalysts and (B) CuO standard sample.

3.3.8. Py-IR analysis. The properties of acid species on the surface of CuAl-LDO and CuAl-LDO/TiO_2NTs catalysts were investigated by Pyridine Adsorption Fourier-transform Infrared (Py-IR) and the results are presented in Fig. 11. For CuAl-LDO and CuAl-LDO/TiO_2NTs catalysts, both the Brønsted and Lewis acid sites were detected simultaneously over the surface. The bands located at ~1440 cm^{-1}, ~1540 cm^{-1}, 1590 cm^{-1} and 1655 cm^{-1} were corresponded to the Lewis acid sites (~1440 cm^{-1} and 1590 cm^{-1}) and Brønsted acid sites (~1540 cm^{-1} and 1655 cm^{-1}), respectively.[32,33] The bands around 1485 cm^{-1} were assigned to both Brønsted and Lewis

Table 3 The reduction peak attribution, amount of hydrogen consumption and normalized NH_3 desorption amount of catalysts

Catalysts	Reduction temperature (°C)		H_2 consumption[a] (mmol g^{-1})	Total amount of NH_3 desorption[b]
	T_1	T_2		
CuAl-LDO	190	240	1.3	1
CuAl-LDO/TiO_2	285	327	1.4	1.7
CuAl-LDO/TiO_2NTs	224	271	1.5	2.7

[a] The H_2 consumption of catalysts was calculated with CuO standard sample. [b] Normalized by the NH_3 total desorption peak area of CuAl-LDO.

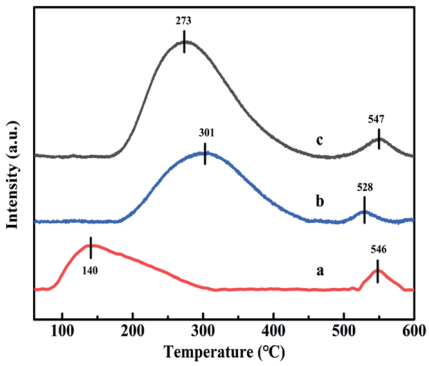

Fig. 10 The NH_3-TPD profiles of catalysts: (a) CuAl-LDO, (b) CuAl-LDO/TiO_2 and (c) CuAl-LDO/TiO_2NTs.

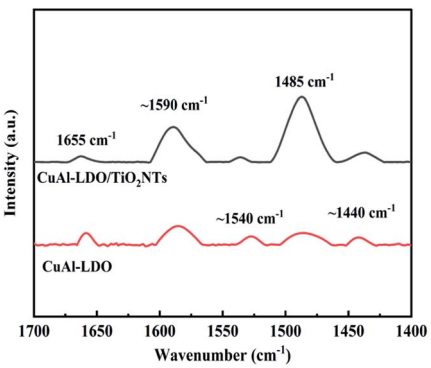

Fig. 11 Py-IR spectra of CuAl-LDO catalyst and CuAl-LDO/TiO_2NTs catalyst.

acid sites over catalysts.[34] The literature was reported that there was only Lewis acid sites over the anatase (TiO_2).[32,33,35] Therefore, the intensity of the band of the Lewis acid sites over CuAl-LDO/TiO_2NTs catalyst was stronger than CuAl-LDO catalyst. In addition, compared with CuAl-LDO, CuAl-LDO/TiO_2NTs catalyst have the most abundant and strongest acid sites over the surface, which was in good agreement with their NH_3-TPD results.

3.4. *In situ* DRIFTS analysis

3.4.1. Adsorption of NH_3. The capacity of NH_3 adsorption over CuAl-LDO and CuAl-LDO/TiO_2NTs catalysts were studied by *In situ* DRIFTS measurement. As shown in Fig. 12(a), for CuAl-LDO catalyst, the bands appeared at 1770–1640 cm^{-1}, 1458 cm^{-1} and 1421 cm^{-1} could be assigned to NH_4^+ species on Brønsted acid sites.[36,37] The peaks of coordinated NH_3 linked to Lewis acid sites were observed at 1621 cm^{-1}, 1543 cm^{-1} and 1228 cm^{-1}.[38] And the bands located at 1513 cm^{-1} and 1390 cm^{-1} were attributed to the –NH_2 scissoring and wagging of N_2H_4 species, separately.[16,39] The peaks for CuAl-LDO/TiO_2-NTs catalyst (in Fig. 12(b)) at 1692 cm^{-1}, 1620 cm^{-1}, 1545 cm^{-1}, 1517 cm^{-1}, 1461 cm^{-1}, 1422 cm^{-1}, 1393 cm^{-1} and 1218 cm^{-1} could be correspondingly assigned to the symmetric and asymmetric vibration of NH_3 species adsorbed on Lewis acid sites (1620 cm^{-1}, 1545 cm^{-1} and 1218 cm^{-1}), the –NH_2 scissoring and wagging of N_2H_4 species (1517 cm^{-1} and 1393 cm^{-1}) and NH_4^+ ions bounded on Brønsted acid site (1692 cm^{-1}, 1461 cm^{-1} and 1422 cm^{-1}).[16,38,40] It could be concluded that the Lewis acid sites and Brønsted acid sites coexisted on the surface of both catalysts. In Fig. 12, it could be found that the peak

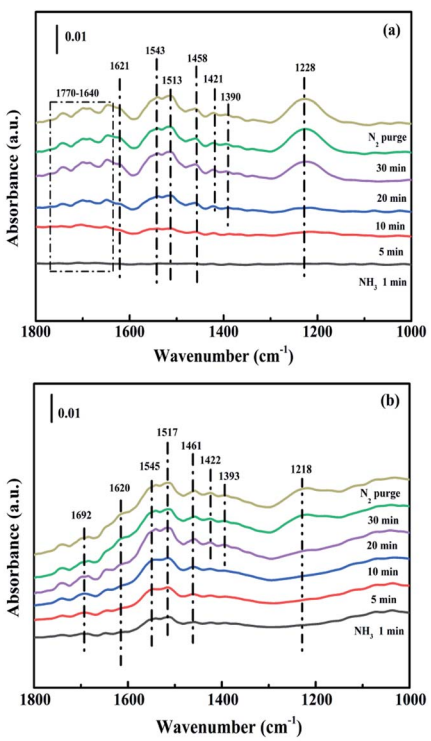

Fig. 12 *In situ* DRIFTS spectra of NH_3 adsorption at 240 °C over (a) CuAl-LDO and (b) CuAl-LDO/TiO_2NTs catalysts.

intensity of the bands assigned to Brønsted acid sites and Lewis acid sites of CuAl-LDO/TiO_2NTs catalyst was higher than that of the CuAl-LDO catalyst, indicating the better NH_3 adsorption capacity of CuAl-LDO/TiO_2NTs catalyst.[13]

3.4.2. Co-adsorption of NO and O_2. *In situ* DRIFTS experiments of NO + O_2 adsorption were applied to research the formation and transformation of NO_x species over the CuAl-LDO and CuAl-LDO/TiO_2NTs catalysts. In Fig. 13(a), the bands at 1271 cm^{-1}, 1240 cm^{-1} and 1135 cm^{-1} were detected for CuAl-LDO catalyst, which could be ascribed to linear nitrite (1454 cm^{-1}), monodentate nitrite (1271 cm^{-1} and 1135 cm^{-1}) and bridged nitrate (1240 cm^{-1}), respectively.[36,41] For CuAl-LDO/TiO_2NTs catalyst, the bands located at 1745–1700 cm^{-1}, 1646 cm^{-1}, 1547 cm^{-1}, 1516 cm^{-1}, 1455 cm^{-1}, 1424 cm^{-1}, 1393 cm^{-1}, 1232 cm^{-1} and 1108 cm^{-1} could be assigned to the absorbed N_2O_4 (1745–1700 cm^{-1}), bridged nitrate (1646 cm^{-1} and 1232 cm^{-1}), bidentate nitrate (1547 cm^{-1} and 1516 cm^{-1}), linear nitrite (1455 cm^{-1}), monodentate nitrite (1424 cm^{-1}, 1393 cm^{-1} and 1108 cm^{-1}).[16,36,41,42] The intensity of peak located at 1232 cm^{-1} was gradually decreased along with the appearance of the band of monodentate nitrate (1262 cm^{-1}). The results displayed that the intensity of NO_x adsorbed peaks over CuAl-LDO/TiO_2NTs were higher than CuAl-LDO. It could be concluded that there was larger amount of NO absorbed on the CuAl-LDO/TiO_2NTs catalyst surface and oxidized to a variety of nitrate species, which resulting in the excellent SCR performance.

3.4.3. Reaction between nitrogen oxides and ammonia adspecies. In order to explore the potential reaction species and possible pathway, the transient reactions between NH_3 and NO + O_2 over CuAl-LDO and CuAl-LDO/TiO_2NTs catalysts were further carried out at 240 °C. As shown in Fig. 14(a), the CuAl-LDO catalyst was firstly absorbed with NH_3 for 30 min. The peaks located at 1770–1640 cm^{-1}, 1458 cm^{-1} and 1421 cm^{-1} (NH_4^+ species on Brønsted acid sites), 1621 cm^{-1}, 1543 cm^{-1} and 1228 cm^{-1} (NH_3 linked to Lewis acid sites) and 1513 cm^{-1} and 1390 cm^{-1} (–NH_2 scissoring and wagging of N_2H_4 species) were detected.[16,36,38,39,43] After inletting NO + O_2 for 10 min, except for the peak located at 1228 cm^{-1}, other peaks almost disappeared, might propose the reaction between adsorbed NH_3 species and NO_x species. After imported NO + O_2 for 20 min, the news bands located at 1721 cm^{-1}, 1667 cm^{-1}, 1621 cm^{-1}, 1596 cm^{-1}, 1484 cm^{-1}, 1440 cm^{-1} and 1136 cm^{-1} appeared which could be assigned to the absorbed N_2O_4 (1721 cm^{-1}), bridged nitrate (1667 cm^{-1}), gaseous NO_2 (1621 cm^{-1}), bidentate nitrate (1596 cm^{-1}), linear nitrite (1440 cm^{-1}), monodentate nitrate (1484 cm^{-1} and 1136 cm^{-1}), respectively.[16,25,36,42] When the reactant gases were introduced as reverse order, the corresponding results are displayed in Fig. 14(c). As can be seen, the pre-adsorption of NO + O_2 lead to the formation of linear nitrite (1454 cm^{-1}), monodentate nitrite (1271 cm^{-1} and 1135 cm^{-1}) and bridged nitrate (1240 cm^{-1}), respectively. The further introduction of NH_3 caused the generation of peaks located at 1770–1640 cm^{-1}, 1458 cm^{-1} and 1421 cm^{-1} (NH_4^+ species on Brønsted acid sites), 1621 cm^{-1}, 1543 cm^{-1} and 1228 cm^{-1} (coordinated NH_3 linked to Lewis acid sites) and 1513 cm^{-1} (–NH_2 scissoring of N_2H_4 species) were detected.[41,44,45] It was worth noting that the intensity of peak located at 1240 cm^{-1} ascribed to bridged nitrite further increased after introducing NH_3, which might be due to the coverage of coordinated NH_3 linked to Lewis acid sites (1228 cm^{-1}). The results indicated that the Eley–Rideal (E–R) mechanisms and Langmuir–Hinshelwood (L–H) mechanisms were occurred simultaneously over the surface of CuAl-LDO catalysts at 240 °C, and the E–R mechanisms were the main reaction way.

While for CuAl-LDO/TiO_2NTs catalysts, the transient reaction spectra are displayed in Fig. 14(b) and (d). After pre-adsorption of NH_3, the following bands emerged, NH_4^+ ions bounded on Brønsted acid site (1692 cm^{-1}, 1461 cm^{-1} and 1422 cm^{-1}), the symmetric and asymmetric vibration of NH_3 species adsorbed on Lewis acid sites (1620 cm^{-1}, 1545 cm^{-1} and 1218 cm^{-1}), the –NH_2 scissoring and wagging of N_2H_4 species (1517 cm^{-1} and 1393 cm^{-1}).[16,39,46] Further importing NO + O_2, the intensity of all peaks gradually impaired, replaced by the arising of peak located at 1237 cm^{-1} corresponding to monodentate nitrate species. In comparison with the Fig. 13(b), there was no significant accumulation of nitrate species participating in the NH_3-SCR reaction. When the reactant gases were introduced as the inverse order, the results are presented in Fig. 14(d). While NO + O_2 were imported for 30 min, the corresponding species appeared as follows: the absorbed N_2O_4 (1745–1700 cm^{-1}), bridged nitrate (1646 cm^{-1} and 1232 cm^{-1}), bidentate nitrate (1547 cm^{-1} and 1516 cm^{-1}), linear nitrite (1455 cm^{-1}), monodentate nitrite (1424 cm^{-1}, 1393 cm^{-1} and 1108 cm^{-1}), monodentate nitrate (1262 cm^{-1}).[16,25,42,47] With an increase in the adsorption time of NH_3, the bands of NO_x species gradually reduced (1745–1700 cm^{-1}, 1646 cm^{-1},

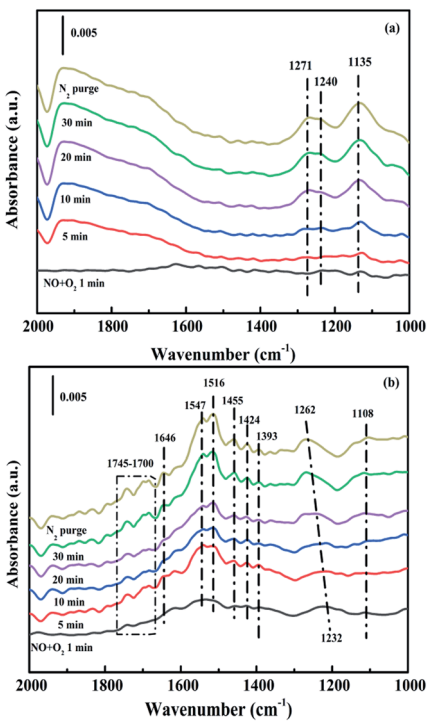

Fig. 13 *In situ* DRIFTS spectra of NO + O_2 adsorption at 240 °C over (a) CuAl-LDO and (b) CuAl-LDO/TiO_2NTs catalyst.

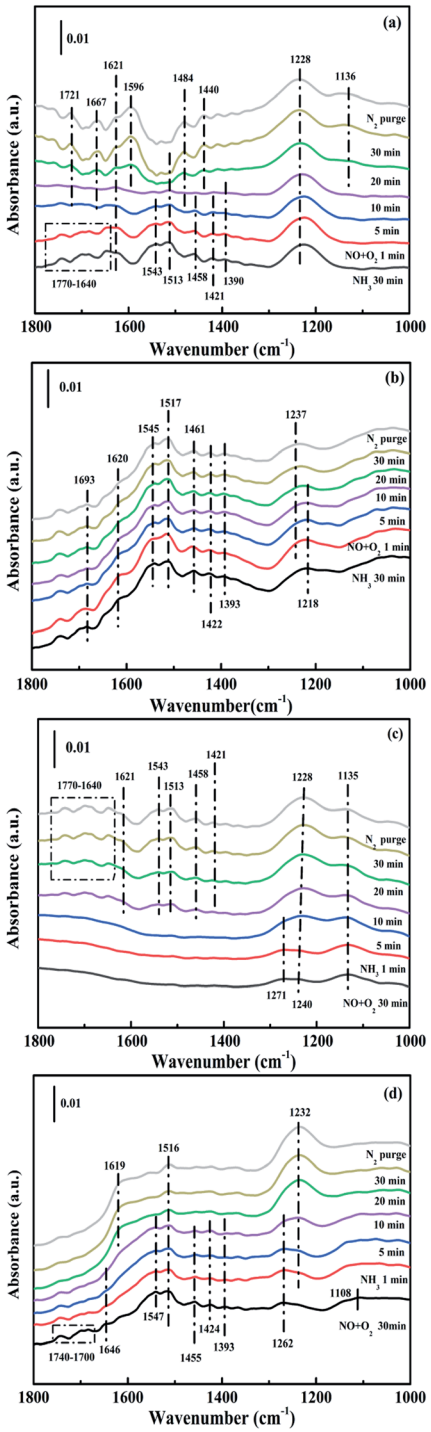

Fig. 14 *In situ* DRIFTS spectra of (a and b) NO + O_2 adsorption with pre-absorbed NH_3 and (c and d) NH_3 adsorption with pre-absorbed NO + O_2 at 240 °C over (a and c) CuAl-LDO and (b and d) CuAl-LDO/TiO_2NTs catalysts.

1547 cm^{-1}, 1455 cm^{-1}, 1424 cm^{-1}, 1393 cm^{-1} 1262 cm^{-1} and 1108 cm^{-1}), accompanied by the emergence of bands located at 1619 cm^{-1} and 1232 cm^{-1}, which were consistent with the asymmetric and symmetric bending vibrations of NH_3 adsorbed on Lewis acid sites (1619 cm^{-1} and 1232 cm^{-1}).[13,48]

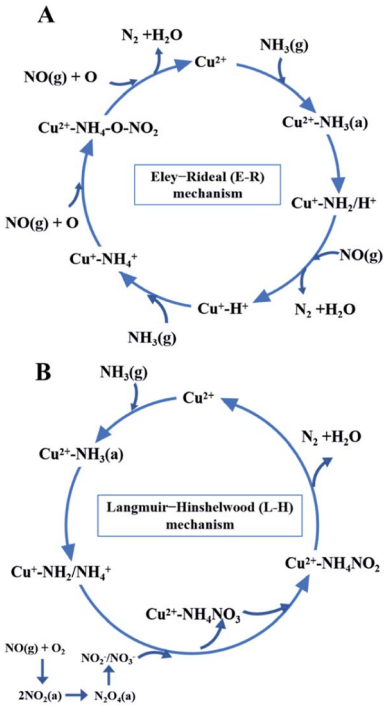

Fig. 15 The NH_3-SCR reaction mechanisms over CuAl-LDO/TiO_2NTs catalyst.

Consequently, the NH_3 species absorbed on the Lewis acid sites could react with nitrate and nitrite species on the surface of CuAl-LDO/TiO_2NTs catalyst in the SCR reaction. The results indicated that CuAl-LDO/TiO_2NTs catalysed the SCR reaction in both E–R mechanism and L–H mechanism. Based on *In situ* DRIFTS, the reaction mechanisms for CuAl-LDO/TiO_2NTs catalyst were proposed, which was displayed in Fig. 15.

4 Conclusions

In summary, CuAl-LDO, CuAl-LDO/TiO_2 and CuAl-LDO/TiO_2-NTs catalysts were obtained by calcining the LDHs precursor, and then applied in NH_3-SCR reaction. The results demonstrated that the introduction of TiO_2NTs with hollow tubular structure effectively avoided the stacking and accumulation of laminates during calcination process and enhanced the number of acidic sites on the catalyst. Consequently, the CuAl-LDO/TiO_2NTs catalyst showed excellent NO_x conversion, N_2 selectivity as well as the good SO_2 resistance. XRD results illustrated that a new phase of Cu_2O was formed in the CuAl-LDO/TiO_2NTs catalyst. Other characterization results indicated that the excellent deNO_x performance of the CuAl-LDO/TiO_2NTs catalyst depended on the synergistic effect between CuO and Cu_2O, which could contribute to the larger surface area, more acidic sites, better redox performance, more abundant surface chemisorption oxygen species and stronger adsorption capacity of reactant gases. This work presents the preparation of Cu-based catalysts with wide temperature window *via* modifying LDHs template, which might serve as an important reference for LDHs precursor to be tailored in NH_3-SCR filed.

Author contributions

Yali Du: validation, formal analysis, writing – review & editing, funding acquisition. Xuezhen Liu: methodology, formal analysis, investigation, resources, data curation, writing – original draft. Jiangning Liu: writing – review & editing, formal analysis. Rongting Du: writing – review & editing. Xu Wu: conceptualization, funding acquisition, project administration, supervision.

Conflicts of interest

There are no conflicts to declare.

Acknowledgements

This work was supported by the National Natural Science Foundation of China (51978436), the National Natural Science Foundation of China (52000092), the Natural Science Foundation of Shanxi Province, China (201901D211445) and China Postdoctoral Science Foundation (2020M670706).

References

1 D. Damma, P. Ettireddy, B. Reddy and P. Smirniotis, *Catalysts*, 2019, **9**, 349.
2 V. Praveena and M. L. J. Martin, *J. Energy Inst.*, 2018, **91**, 704–720.
3 M. Fu, C. Li, P. Lu, L. Qu, M. Zhang, Y. Zhou, M. Yu and Y. Fang, *Catal. Sci. Technol.*, 2014, **4**, 14–25.
4 Q. Yan, S. Chen, L. Qiu, Y. Gao, D. O'Hare and Q. Wang, *Dalton Trans.*, 2018, **47**, 2992–3004.
5 W. Wang, Z. Xiong, W. He, W. Lu and H. Shi, *J. Energy Inst.*, 2021, **98**, 322–333.
6 C. Chen, Y. Cao, S. Liu, J. Chen and W. Jia, *Chin. J. Catal.*, 2018, **39**, 1347–1365.
7 Z. Song, Y. Xing, X. Zhang, H. Zhao, M. Zhao, J. Zhao, Z. Ma and Q. Zhang, *Appl. Organomet. Chem.*, 2019, **33**, e5160.
8 C. Li, Z. Xiong, Y. Du, X. Ning, Z. Li, J. He, X. Qu, W. Lu, S. Wu and L. Tan, *J. Energy Inst.*, 2020, **93**, 1809–1818.
9 S. Zang, G. Zhang, W. Qiu, L. Song, R. Zhang and H. He, *Chin. J. Catal.*, 2016, **37**, 888–897.
10 Z. Fan, J.-W. Shi, C. Gao, G. Gao, B. Wang, Y. Wang, C. He and C. Niu, *Chem. Eng. J.*, 2018, **348**, 820–830.
11 K. Cheng, W. Song, Y. Cheng, H. Zheng, L. Wang, J. Liu, Z. Zhao and Y. Wei, *RSC Adv.*, 2018, **8**, 19301–19309.
12 B. Hou, Y. Du, X. Liu, C. Ci, X. Wu and X. Xie, *RSC Adv.*, 2019, **9**, 24377–24385.
13 S. Ali, L. Chen, Z. Li, T. Zhang, R. Li, S. H. Bakhtiar, X. Leng, F. Yuan, X. Niu and Y. Zhu, *Appl. Catal. B Environ.*, 2018, **236**, 25–35.
14 X. Gao, X. Du, L. Cui, Y. Fu, Z. Luo and K. Cen, *Catal. Commun.*, 2010, **12**, 255–258.
15 S. Suárez, J. A. Martín, M. Yates, P. Avila and J. Blanco, *J. Catal.*, 2005, **229**, 227–236.
16 X. Yao, L. Zhang, L. Li, L. Liu, Y. Cao, X. Dong, F. Gao, Y. Deng, C. Tang, Z. Chen, L. Dong and Y. Chen, *Appl. Catal. B Environ.*, 2014, **150–151**, 315–329.
17 X. Wu, R. Wang, Y. Du, C. Zou, H. Meng and X. Xie, *Mol. Catal.*, 2019, **467**, 150–160.
18 X. Wu, H. Meng, Y. Du, J. Liu, B. Hou and X. Xie, *J. Catal.*, 2020, **384**, 72–87.
19 Q. Yan, Y. Nie, R. Yang, Y. Cui, D. O'Hare and Q. Wang, *Appl. Catal. Gen.*, 2017, **538**, 37–50.
20 R. Fan, Z. Li, Y. Wang, C. Zhang, Y. Wang, Z. Ding, X. Guo and R. Wang, *RSC Adv.*, 2020, **10**, 5845–5852.
21 D. K. Pappas, T. Boningari, P. Boolchand and P. G. Smirniotis, *J. Catal.*, 2016, **334**, 1–13.
22 S.-A. Chen, J.-N. Nian, C.-C. Tsai and H. Teng, *J. Air Waste Manage. Assoc.*, 2007, **57**, 600–605.
23 Z. Cai, G. Zhang, Z. Tang and J. Zhang, *ACS Appl. Nano Mater.*, 2021, **4**, 6201–6211.
24 C. Liu, L. Chen, J. Li, L. Ma, H. Arandiyan, Y. Du, J. Xu and J. Hao, *Environ. Sci. Technol.*, 2012, **46**, 6182–6189.
25 D. Meng, W. Zhan, Y. Guo, Y. Guo, L. Wang and G. Lu, *ACS Catal.*, 2015, **5**, 5973–5983.
26 Z. He, H. Lin, P. He and Y. Yuan, *J. Catal.*, 2011, **277**, 54–63.
27 L. Dou, T. Fan and H. Zhang, *Catal. Sci. Technol.*, 2015, **5**, 5153–5167.
28 Y. Geng, W. Shan, F. Liu and S. Yang, *J. Hazard. Mater.*, 2021, **405**, 124223.
29 M. Ma, R. Yang, Z. Jiang, C. Chen, Q. Liu, R. Albilali and C. He, *Fuel*, 2021, **303**, 121244.
30 Q. Yan, Y. Gao, Y. Li, M. A. Vasiliades, S. Chen, C. Zhang, R. Gui, Q. Wang, T. Zhu and A. M. Efstathiou, *Appl. Catal. B Environ.*, 2019, **255**, 117749.
31 J. Zhang, H. Tian, Y. Yu, Z. Jiang, M. Ma and C. He, *Catal. Lett.*, 2021, **151**, 2502–2512.
32 Y. Liu, Y. Guan, C. Li, J. Lian, G. Gan, E. Lim and F. Kooli, *J. Catal.*, 2006, **244**, 17–23.
33 L. Sun, S. Cao, Y. Huang, Y. Zhang, Y. Xiao, G. Dong and Y. Su, *RSC Adv.*, 2019, **9**, 30340–30349.
34 W. Yao, Y. Liu, X. Wang, X. Weng, H. Wang and Z. Wu, *J. Phys. Chem. C*, 2016, **120**, 221–229.
35 L. Li, H. Yue, T. Ji, W. Li, X. Zhao, L. Wang, J. She, X. Gu and X. Li, *Appl. Catal. Gen.*, 2019, **574**, 25–32.
36 L. Chen, Z. Si, X. Wu and D. Weng, *ACS Appl. Mater. Interfaces*, 2014, **6**, 8134–8145.
37 Q. Zhang, T. Zhang, F. Xia, Y. Zhang, H. Wang and P. Ning, *Appl. Surf. Sci.*, 2020, **500**, 144044.
38 J. Ma, Y. Li, J. Liu, Z. Zhao, C. Xu, Y. Wei, W. Song, Y. Sun and X. Zhang, *Ind. Eng. Chem. Res.*, 2019, **58**, 2389–2395.
39 C. Yu, B. Huang, L. Dong, F. Chen and X. Liu, *Catal. Today*, 2017, **281**, 610–620.
40 Y. Wei, P. Zhang, J. Xiong, Q. Yu, Q. Wu, Z. Zhao and J. Liu, *Environ. Sci. Technol.*, 2020, **54**, 6947–6956.
41 H. Hu, S. Cai, H. Li, L. Huang, L. Shi and D. Zhang, *J. Phys. Chem. C*, 2015, **119**, 22924–22933.
42 G. Zhou, B. Zhong, W. Wang, X. Guan, B. Huang, D. Ye and H. Wu, *Catal. Today*, 2011, **175**, 157–163.
43 T. Zhang, R. Qu, W. Su and J. Li, *Appl. Catal. B Environ.*, 2015, **176–177**, 338–346.

44 L. Wei, S. Cui, H. Guo, X. Ma and L. Zhang, *J. Mol. Catal. Chem.*, 2016, **421**, 102–108.
45 Z. Zhang, L. Chen, Z. Li, P. Li, F. Yuan, X. Niu and Y. Zhu, *Catal. Sci. Technol.*, 2016, **6**, 7151–7162.
46 R. Gao, D. Zhang, X. Liu, L. Shi, P. Maitarad, H. Li, J. Zhang and W. Cao, *Catal. Sci. Technol.*, 2013, **3**, 191–199.
47 Y. Wen, S. Cao, X. Fei, H. Wang and Z. Wu, *Chin. J. Catal.*, 2018, **39**, 771–778.
48 Z. Liu, H. Liu, X. Feng, L. Ma, X. Cao and B. Wang, *Mol. Catal.*, 2018, **445**, 179–186.